PHYSICAL REVIEW B **76**, 104415 (2007)

Quantum-well state induced oscillations of the electron-spin motion in Au films on Co(001)

L. Joly, L. Tati Bismaths, F. Scheurer, and W. Weber
Institut de Physique et Chimie des Matériaux de Strasbourg, UMR 7504, ULP-CNRS 23 rue du Loess, BP 43, F-67034 Strasbourg Cedex 2, France

(Received 29 May 2007; revised manuscript received 27 July 2007; published 14 September 2007)

We report on spin-polarized electron reflection experiments in which the electron-spin motion is studied in spin-dependent quantum-well structures. Quantum-well state induced oscillations of both the electron reflectivity and the electron-spin motion are observed in the system Au/Co(001) as a function of the Au overlayer thickness. A Fabry-Pérot interferometer model can explain the main features of the experimental data. We discuss the influence of the spin-dependent reflectivity, the inelastic mean free path, the diffusively scattered electron intensity contribution, and the growth mode on the behavior of the electron-spin motion within the interferometer model.

DOI: 10.1103/PhysRevB.76.104415 PACS number(s): 72.25.Mk, 75.70.Cn, 78.67.De

I. INTRODUCTION

Once the existence of quantum-well states in thin metallic films was clearly established, a number of different oscillatory phenomena could be explained by their presence.[1] In particular, in systems such as Au/Co, one partner is ferromagnetic so that the existence of a magnetic interface results in a spin dependence of the quantum confinement. The latter is responsible for oscillations of the exchange coupling between two ferromagnetic layers separated by a nonmagnetic spacer layer,[2] of the magneto-optical response,[3] of the induced magnetic moment,[4] and of the magnetic anisotropy.[5] Very recently also oscillations of the electron-spin motion due to the existence of spin-dependent quantum-well states have been observed in Cu films on Co(001).[6] Moreover, both the electron reflectivity and the electron-spin motion could be well described within a Fabry-Pérot interferometer model which opened, in particular, the possibility of studying the spin-dependent reflection properties of the buried Cu/Co interface.

In order to test the general applicability of the interferometer model, we set out to study another system, namely, Au films on Co(001). We note that it was in Au films that quantum-well size effects were observed for the first time in metallic films by reflection of low-energy electrons.[7] Although we are dealing here with the same ferromagnet, Co(001), the choice of Au as overlayer material leads to a quite different situation than in the case of Cu. First, the electron reflectivities are very different. It turns out that for low electron kinetic energies, the reflectivity of the Au/Co interface is much larger than that of the vacuum/Au interface. Such a situation could not be realized in the Cu/Co system. Second, the inelastic mean free path of the electrons in Au at low kinetic energies is much larger than in Cu. These two points lead, as we will see in the following, to a different behavior of the electron-spin precession as in our recent study of the Cu/Co system.[6] Third, while diffusively scattered electrons having arbitrary phase were of no importance in the discussion of the Cu/Co system, they become crucial for the understanding of the experimental electron-spin motion data of the Au/Co system.

II. ELECTRON-SPIN MOTION

In the following, the spin polarization vector $\vec{P}_0$ of the incident electron beam is perpendicular to the direction of the magnetization $\vec{M}$ of the ferromagnetic film. It is only with this noncollinear initial configuration that the electron-spin motion can be observed.[8–12] We note that, in this paper, the direction of $\vec{M}$ is that of the majority spins.

For simplicity, we consider now a completely polarized electron beam, i.e., $P_0=100\%$. The spin polarization vector $\vec{P}$ is given by the expectation values of the Pauli matrices σ_i ($i=x,y,z$):

$$\vec{P}=\frac{\langle\chi|\vec{\sigma}|\chi\rangle}{\langle\chi|\chi\rangle}, \tag{1}$$

where χ is the spin wave function of the completely polarized electron beam. The initial spin polarization $\vec{P}_0$ is along the x axis, i.e., $\vec{P}_0=(1,0,0)$, and the electron beam interacts with a ferromagnetic system that is magnetized along the z axis (see Fig. 1). The spin wave function χ_0 of the incident electrons, which in this case is an eigenstate of the σ_x operator, is represented by a superposition of a majority-spin wave function $\binom{1}{0}$ (eigenstate of the σ_z operator with the spin parallel to $\vec{M}$) and a minority-spin wave function $\binom{0}{1}$ (eigenstate of the σ_z operator with the spin antiparallel to $\vec{M}$):

$$\chi_0=\frac{1}{\sqrt{2}}\begin{pmatrix}1\\1\end{pmatrix}e^{i\gamma}=\frac{1}{\sqrt{2}}\left[\begin{pmatrix}1\\0\end{pmatrix}+\begin{pmatrix}0\\1\end{pmatrix}\right]e^{i\gamma}. \tag{2}$$

The two partial wave functions have an arbitrary but identical phase γ prior to the reflection. After reflection, because of the spin dependence of the reflection process, the amplitudes of the two spin wave functions become different. Thus, the spin wave function representing the electrons reflected from the ferromagnetic system is

$$\chi=\frac{1}{\sqrt{2}}\left[|r^{\uparrow}|e^{i\theta^{\uparrow}}\begin{pmatrix}1\\0\end{pmatrix}+|r^{\downarrow}|e^{i\theta^{\downarrow}}\begin{pmatrix}0\\1\end{pmatrix}\right]e^{i\gamma}, \tag{3}$$

where $|r^{\uparrow,\downarrow}|$ and $\theta^{\uparrow,\downarrow}$ are respectively the moduli and the phases of the spin-dependent reflection amplitudes. The com-

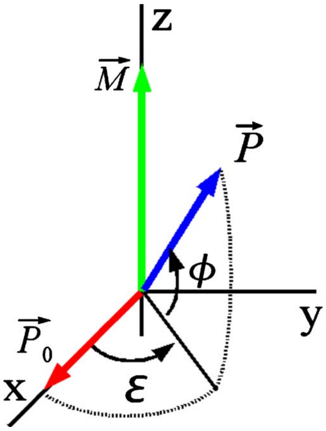

FIG. 1. (Color online) The two types of movement of the spin polarization vector: a precession about the magnetization $\vec{M}$ by an angle ε and a rotation by an angle ϕ in the plane spanned by $\vec{P}$ and $\vec{M}$.

ponents of the spin polarization vector of the reflected electron beam are thus

$$P_x = \frac{2|r^{\uparrow}||r^{\downarrow}|\cos(\theta^{\downarrow}-\theta^{\uparrow})}{|r^{\uparrow}|^2+|r^{\downarrow}|^2}, \tag{4}$$

$$P_y = \frac{2|r^{\uparrow}||r^{\downarrow}|\sin(\theta^{\downarrow}-\theta^{\uparrow})}{|r^{\uparrow}|^2+|r^{\downarrow}|^2}, \tag{5}$$

$$P_z = \frac{|r^{\uparrow}|^2-|r^{\downarrow}|^2}{|r^{\uparrow}|^2+|r^{\downarrow}|^2}. \tag{6}$$

This corresponds to a precession of the polarization vector around $\vec{M}$ by an angle

$$\varepsilon = \theta^{\downarrow} - \theta^{\uparrow} \tag{7}$$

and a rotation by an angle ϕ in the plane spanned by $\vec{P}$ and $\vec{M}$ (see Fig. 1). Taking into account the incomplete spin polarization of the incident electron beam in the experiment, one obtains

$$\phi = \arctan\left(\frac{|r^{\uparrow}|^2-|r^{\downarrow}|^2}{2P_0|r^{\uparrow}||r^{\downarrow}|}\right). \tag{8}$$

In the following, the values of ϕ are normalized to a fully polarized incident electron beam.

III. EXPERIMENT: SPIN-POLARIZED ELECTRON REFLECTION

The experimental setup is sketched in Fig. 2. A 70% spin-polarized free electron beam is produced by optical pumping of a strained GaAs-type photocathode with circularly polarized light. By switching from right- to left-circularly polarized light for excitation of the photoelectrons, we can invert the direction of the initial polarization vector $\vec{P}_0$. By applying a combination of electric and magnetic fields to the electron beam, $\vec{P}_0$ can also be rotated into any desired direction in space, in particular, in a direction perpendicular to the magnetization $\vec{M}$. The spin-polarized electron beam impinges onto the quantum-well structure under an angle of 45° with respect to the surface normal. The ferromagnetic Co film is remanently magnetized along the easy direction of magnetization (the [110] direction) by applying a magnetic field pulse. The specularly reflected electrons are energy analyzed by a retarding grid analyzer with an energy resolution of ±0.25 eV. Besides the elastic electrons, there is a broad distribution of inelastic electrons as well. However, in the following, we restrict ourselves to the discussion of the elastic electrons which can be separated by applying a retarding field. The electrons are subsequently accelerated to an energy of 100 keV to measure the transverse components of the spin polarization vector via Mott scattering. We note that the component of the spin polarization vector along the propagation direction of the electrons cannot be measured by our experimental setup. However, by exploiting the different symmetries of the two spin-motion angles with respect to an inversion of $\vec{P}_0$ and $\vec{M}$, the spin motion can be determined without directly measuring the component of the spin polarization vector along the axis of the reflected beam. This technique in which both the absolute direction of $\vec{P}_0$ and $\vec{M}$ as well as their relative orientation are changed also eliminates the effects of the spin-orbit interaction, which is supposed to be quite strong in Au.

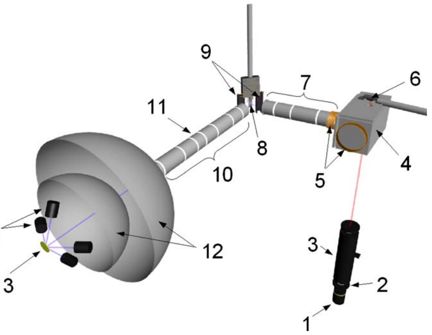

FIG. 2. (Color online) Scheme of the experiment. 1, laser; 2, polarizer; 3, Pockels cell (to create circularly polarized light and to change its helicity); 4, electrostatic 90° deflector; 5, coils to rotate $\vec{P}_0$; 6, strained GaAs-type crystal; 7, transfer electron optics; 8, sample; 9, coils to remanently magnetize the sample; 10, transfer electron optics; 11, retarding field grid (as energy analyzer); and 12–14, spin detectors (12, accelerator; 13, Au foil for Mott scattering; and 14, detectors).

IV. FILM SYSTEM Au/Co(001)

The system consists in a Au/Co sandwich deposited on Cu(001). Prior to film preparation, the Cu(001) single crystal was cleaned by sputtering and subsequent annealing to 800 K. The thick Co film was grown by molecular beam epitaxy at room temperature. Au was deposited onto the Co(001) film at room temperature with a growth rate of 0.05 nm/min. The growth mode of Au on Co was studied by

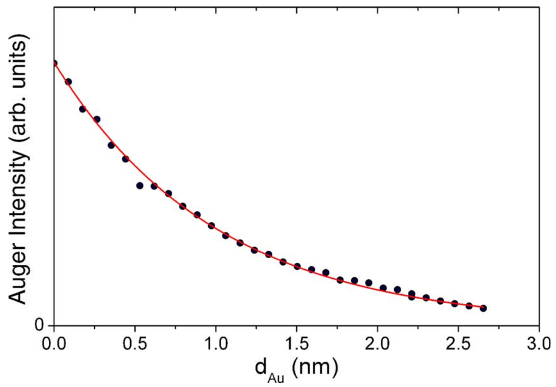

FIG. 3. (Color online) The intensity of the Co Auger line (peak-to-peak height) at 775 eV as a function of film thickness for Au growth on Co/Cu(001). The line is an exponential fit to the data.

analyzing the intensity decrease of the 775 eV Co Auger peak as a function of Au thickness (see Fig. 3), which was measured within an accuracy of about 10% with a calibrated quartz microbalance. Deposition of Au was periodically interrupted and the sample brought to the Auger analysis position. The Auger spectra were recorded with a four-grid low-energy electron diffraction (LEED) optics detecting the Auger electrons under an averaged emission angle of about 34°.

The Auger intensity as a function of thickness (Fig. 3) is well fitted by an exponential decrease of the form

$$I(d_{\mathrm{Au}}) \propto e^{-d/\lambda \cos(34^\circ)}, \tag{9}$$

with λ the attenuation length. A value of $\lambda = 1.25$ nm is found, which is in good agreement with the inelastic mean free path curve given by Seah and Dench.[13] Thus, the decrease of the Co Auger intensity is consistent with a layer-by-layer growth of Au on Co(001). In fact, for a significant deviation from layer-by-layer growth (e.g., clustering), one expects a value of λ from such a fitting procedure that is significantly larger than the inelastic mean free path. A further confirmation that the growth mode is not too far from layer-by-layer growth is the appearance of very pronounced oscillations in the electron-spin motion (see Sec. VI F), which can only be explained by the existence of a sharp Au/Co interface and a narrow height distribution of the Au film.

Whereas the Co film keeps the structure of the Cu(001) substrate [Fig. 4(a)],[14] the Au structure as measured by LEED is very different. For Au coverages as small as 2 ML (monolayer; 1 ML corresponds to 0.233 nm), the LEED pattern has disappeared and is replaced by a strong background intensity. This indicates a highly disordered Au film. At much larger thickness (>18 ML), a LEED pattern appears again, consisting of two 30° rotated hexagonal patterns with elongated spots [Fig. 4(b)]. A similar structure has been obtained for Au/Cu(001).[15] This structure consists of two fcc (111) Au domains, with the Au dense rows being parallel to the dense Co rows, i.e., either [110] or [1$\bar{1}$0]. This structure is characteristic of a unidirectional epitaxial growth, similar to what is obtained, e.g., for a general pitch orientation [where a bcc(110) plane matches a fcc(001) plane]. For such type of epitaxy, there is a fair matching along one surface lattice vector and a bad one along the other vector. The epitaxial domains are, therefore, supposed to be rather small and elongated along the direction where the matching is good, leading to streaks instead of sharp LEED spots (see, e.g., Ref. 16). A quantitative analysis shows that Au has a lattice parameter of about 0.266 nm, which is compressed with respect to its bulk parameter (0.288 nm). Such a small parameter is actually reasonable: the basic gold surfaces present an overdensification and reduced nearest-neighbor distances ranging from 0.265 to 0.285 nm.[17,18]

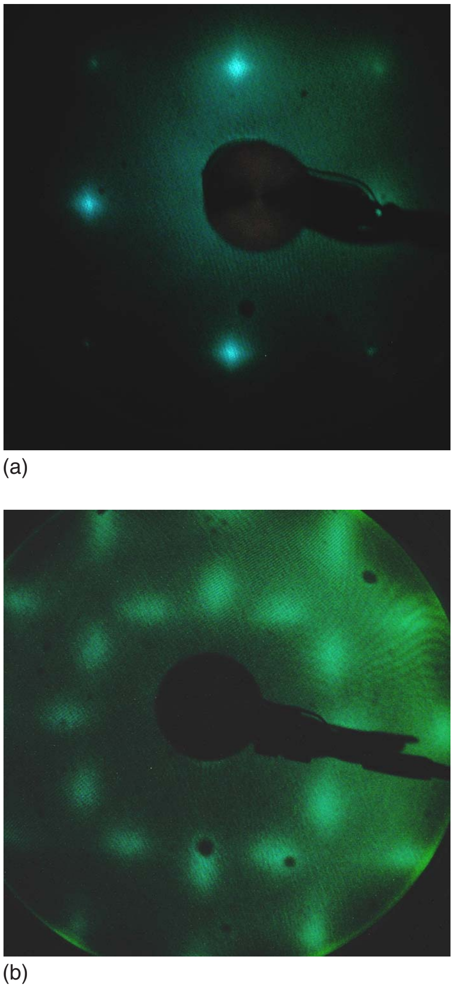

FIG. 4. (Color online) LEED patterns of (a) 28 ML Co/Cu(001) and (b) 34 ML Au on Co/Cu(001). Electron energy: 144 eV. The [110] direction of the Cu(001) single crystal is horizontal.

V. RESULTS

In order to study the effect of quantum-well states on the behavior of the reflected electrons, we measured both the spin-integrated electron reflectivity (see Fig. 5) and the electron-spin motion, i.e., the precession angle ε (see Fig. 6) and the rotation angle ϕ (see Fig. 7), as a function of the Au film thickness for different electron energies. We note that

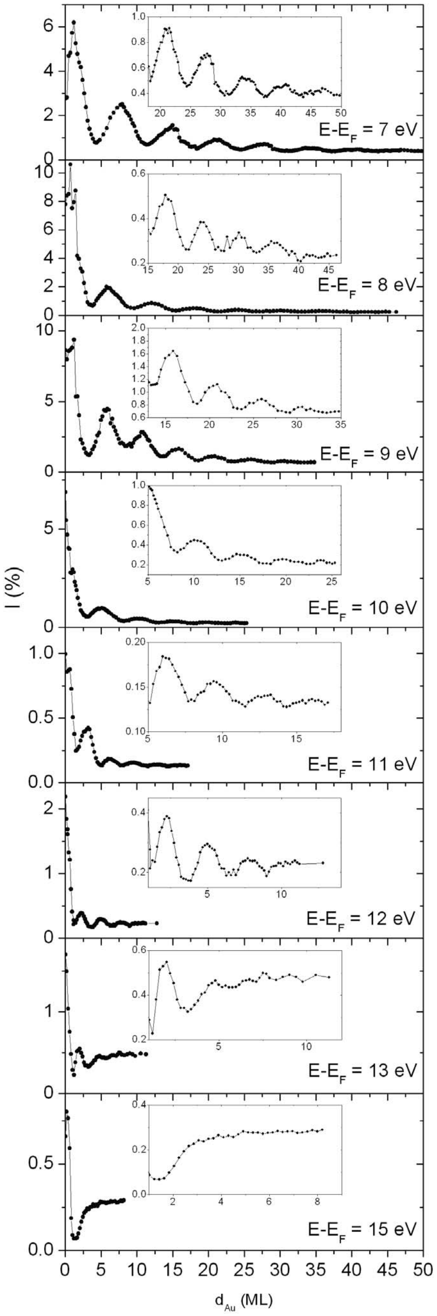

FIG. 5. Quantum-size oscillations of the spin-integrated electron reflectivity I as a function of the Au overlayer thickness for eight different primary electron energies $E-E_F$. The insets are zooms.

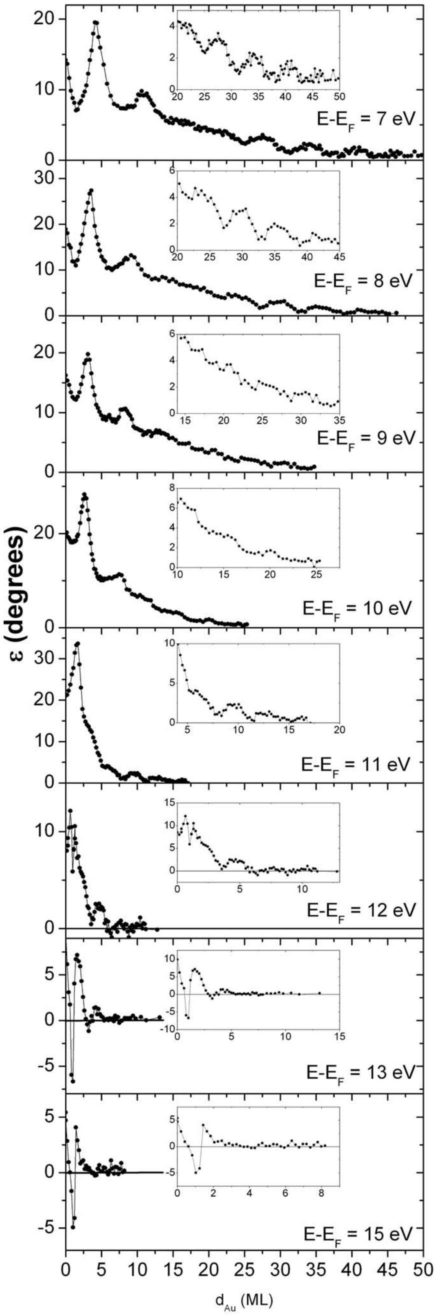

FIG. 6. Quantum-size oscillations of the precession angle ε as a function of the Au overlayer thickness for eight different primary electron energies $E-E_F$. The error in ε is ±0.2°. The insets are zooms.

the time to take a data point was several minutes.

Clear oscillations of the reflectivity are seen and are much more pronounced than in the case of Cu/Co.[6] This enables us to identify at the lowest electron energies up to seven oscillations. With increasing electron energy, both the period and the attenuation strength of the oscillations change. While the period decreases, the attenuation becomes stronger. Finally, for energies above 14 eV, no oscillations can be identified in the reflectivity measurements anymore.

Oscillations of the rotation angle ϕ are also very pronounced. Interestingly, while they are quite symmetric with respect to the abscissa between 7 and 11 eV, they become asymmetric for higher electron energies. As already seen in the reflectivity, both the period and the attenuation strength of the oscillations change drastically with increasing electron energy. The behavior of the precession angle, on the other hand, is quite different from that of the rotation angle. In the electron energy range from 7 to 11 eV, ε takes only positive values while ϕ takes positive as well as negative values. If we compare the positions of the extrema in reflectivity with those in ε, we make a remarkable observation. Let us con-

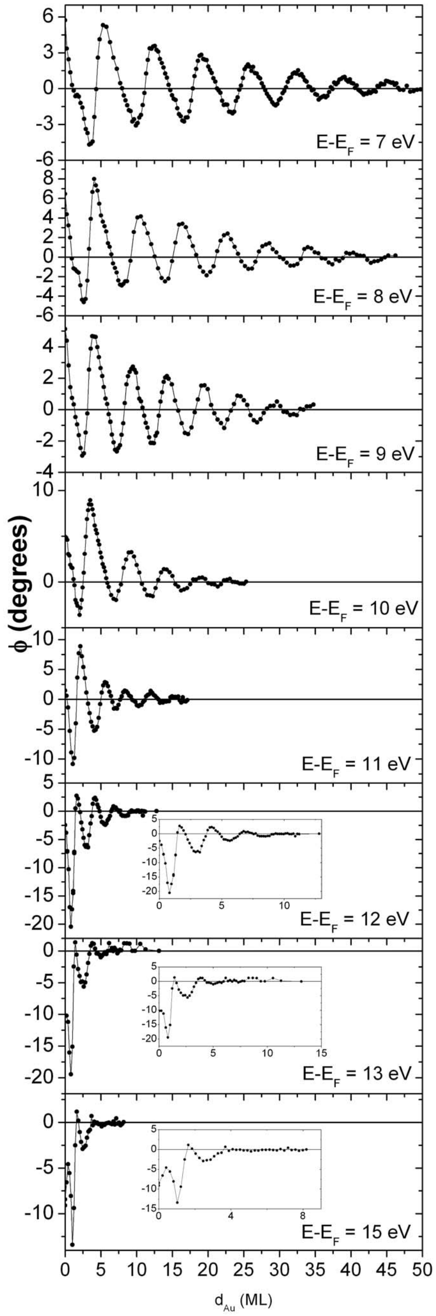

FIG. 7. Quantum-size oscillations of the rotation angle ϕ as a function of the Au overlayer thickness for eight different primary electron energies $E-E_F$. The error in ϕ is ±0.2°. The insets are zooms.

sider, for example, the situation at 7 eV: while the minima in reflectivity at 4 and 11 ML correspond to the first two maxima in ε, the further minima in reflectivity correspond to minima in ε which always take positive values. However, for electron energies above 11 eV, ε takes positive as well as negative values. Moreover, all minima in reflectivity correspond now to minima in ε. We note that extrema of ε appear whenever the rotation angle ϕ shows its strongest change, i.e., there is a phase shift of $\pi/2$ between ε and ϕ.

VI. DISCUSSION

A. Oscillation period and inelastic mean free path

Intensity oscillations as a function of film thickness have been reported both in photoemission and in electron reflection experiments for a number of quantum-well systems.[1] Their appearance is explained by the phase accumulation model.[19] If the electron system is confined to a film of thickness d, constructive interference, i.e., a maximum in reflectivity, requires the wave vector k of the electrons in the film to fulfill the following quantization condition:

$$2kd\cos(\alpha) + \theta_{21} + \theta_{23} = 2\pi n, \tag{10}$$

with θ_{21} and θ_{23} the phase gains of the electron wave function upon reflection at the film/vacuum and the film/substrate interface, respectively, and n an integer specifying the number of half wavelengths which fit into the quantum well. The angle of incidence α of the electrons at the film/substrate interface in our experimental geometry is determined by

$$\sin(\alpha) = \sin(45°)\sqrt{\frac{E_{kin}}{E_{kin}+U}}, \tag{11}$$

with E_{kin} the kinetic energy of the electrons in vacuum and U the inner potential of Au [≈16 eV (Ref. 7)]. It is important to note, however, that the periodicity of the intensity oscillations is, in general, not determined by the wave vector of the oscillating Bloch wave function within the quantum well. In fact, for electron wave vectors close to the Brillouin zone (BZ) boundary ($k \approx k_{BZ}$), it has been proposed that electron waves under this situation should carry an envelope function with wave vector $k_{env}=k_{BZ}-k$ that modulates the fast oscillating Bloch wave function with wave vector k.[20–22] In this case, the above quantization condition has to be rewritten:

$$2k_{env}d\cos(\alpha) - \theta_{21} - \theta_{23} = 2\pi\nu, \tag{12}$$

with the quantum number ν being now the number of half wavelengths of the envelope function fitting into the quantum well.

The period of the envelope function is given by $\Lambda = \pi/k_{env}$ and can be extracted directly from the experimental data without the assumption of a particular model (see Fig. 8). The oscillation period shows a strong increase by going to lower electron energies, a behavior which has also been observed in the system[6,23] Cu/Co(001) and is explained by the presence of a gap in the electronic band structure of Au at lower electron energies. On approaching a band gap, the wave vector $k_{BZ}-k$ of the envelope function becomes smaller and results, thus, in an increase of the oscillation period Λ. In fact, an inspection of the calculated electronic band structure of Au along the Γ-L line in reciprocal space shows us that a band gap exists below $E-E_F=3$ eV.[24] We emphasize that a comparison of the experimental data with a calculated band structure along the Γ-L line is justified. Although the electron beam impinges the Au surface under an angle of 45°, the angle of incidence α in the Au overlayer is much smaller and becomes almost zero for electron energies close to the vacuum level ($E-E_F \approx 5$ eV).

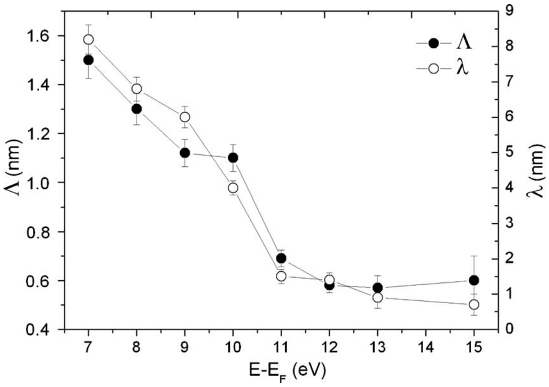

FIG. 8. The period Λ of the quantum-well oscillations and the inelastic mean free path λ as a function of the primary electron energy.

Besides the oscillation period, a further quantity can also be directly extracted from the experimental data, namely, the inelastic mean free path λ which determines—assuming layer-by-layer growth—the attenuation strength of the oscillations (see Fig. 8). A strong decrease with increasing electron energy is observed, and the values at low electron energies are much larger than those found by Kanter for polycrystalline Au films.[25]

B. Fabry-Pérot interferometer model

In order to understand the behavior of the electron-spin motion as a function of Au thickness, we will consider in the following a multiple-reflection model (see Fig. 9) which is analogous to the Fabry-Pérot interferometer model used in optics. However, there is one important difference between an optical interferometer and our electron interferometer. While many reflections must usually be considered in an optical interferometer to describe correctly its behavior, only few reflections are necessary in our electron analog. This is due to the small electron reflectivity as well as to the strong electron attenuation in the investigated electron energy range. In practice, the consideration of one reflection at the film/substrate interface is largely sufficient.

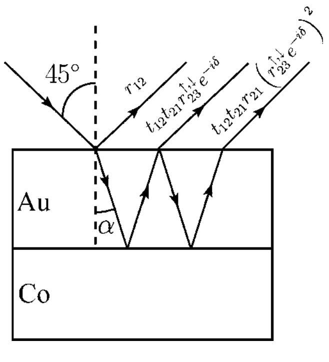

FIG. 9. A simple Fabry-Pérot interferometer model explains the oscillations of the electron reflectivity as well as of the electron-spin motion as interference fringes of electron waves reflected both from the vacuum(1)/Au(2) interface and the Au(2)/Co(3) interface. α is the angle of incidence of the electrons reflected at the Au/Co interface; r_{12}, r_{21}, t_{12}, and t_{21} the spin-independent reflection and transmission amplitudes at the vacuum/Au interface; $r_{23}^{\uparrow,\downarrow}$ the spin-dependent reflection amplitude at the Au/Co interface; and δ a complex phase factor.

Considering N reflections at the Au/Co interface, the total spin-dependent amplitude of the reflected electron wave reads

$$r^{\uparrow,\downarrow} = |r^{\uparrow,\downarrow}|e^{i\theta^{\uparrow,\downarrow}} = r_{12} + t_{12}t_{21}\sum_{k=1}^{N} r_{21}^{k-1}(r_{23}^{\uparrow,\downarrow}e^{-i\delta})^k, \qquad (13)$$

with $r_{12}(=|r_{12}|e^{i\theta_{12}})$, r_{21}, t_{12}, and t_{21} the spin-independent reflection and transmission amplitudes at the vacuum/Au interface (for one spin direction), respectively; $r_{23}^{\uparrow,\downarrow}=|r_{23}^{\uparrow,\downarrow}|e^{i\theta_{23}^{\uparrow,\downarrow}}$ the spin-dependent reflection amplitude at the Au/Co interface with $\theta_{23}^{\uparrow,\downarrow}$ the spin-dependent phase gain [in the following, we will also use the spin-averaged phase $\theta_{23}=(\theta_{23}^{\uparrow}+\theta_{23}^{\downarrow})/2$]; and δ a Au-thickness-dependent complex phase factor. The latter contains the phase difference between two successively reflected electron rays as well as an attenuation factor due to the finite inelastic mean free path λ of the electrons in Au:

$$\delta(d) = 2d\left[\frac{\pi}{\Lambda}\cos(\alpha) - \frac{i}{\lambda\cos(\alpha)}\right]. \qquad (14)$$

We note that the above reflection and transmission amplitudes are not independent of each other and fulfill the following relations: $r_{21}=-r_{12}$, $t_{12}=1+r_{12}$, and $t_{21}=1+r_{21}$.

In order to calculate the reflection amplitude as a function of Au film thickness, we have to assume a certain growth mode. For simplicity, we assume in the following perfect layer-by-layer growth of the Au film on top of the Co(001) substrate. Thus, for a given thickness d, we have to consider, in general, two film regions which differ by 1 ML in thickness. To determine the total signal coming from interferometers having different thicknesses, we will distinguish between two limiting situations: (a) the spatial coherence r_c of the electron beam is much smaller than the typical linear dimension l of the film terraces (i.e., $r_c \ll l$) and (b) the spatial coherence is much larger than the latter (i.e., $r_c \gg l$). We note that in our experimental setup, the spatial coherence of the electron beam is about 5 nm.

1. $r_c \ll l$: Model of independent interferometers

In this model, the interferometers having a thickness of n completely filled monolayers are considered as being independent. The reflectivity, the precession angle, and the rotation angle of the film are, thus, given by

$$I = \sum_{n=1} (c_n - c_{n+1})|r_n|^2, \qquad (15)$$

$$\varepsilon = \frac{1}{I}\sum_{n=1} (c_n - c_{n+1})|r_n|^2\varepsilon_n, \qquad (16)$$

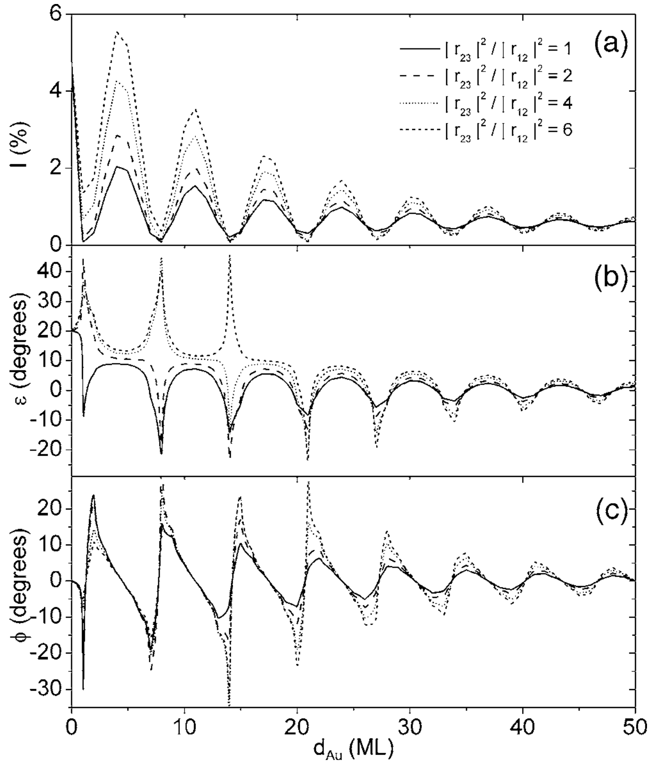

FIG. 10. Fabry-Pérot model with independent interferometers without intensity contribution of diffusively scattered electrons and perfect layer-by-layer growth. (a) The reflectivity I, (b) the precession angle ε, and (c) the rotation angle ϕ are shown as a function of the Au film thickness for different reflectivity ratios $|r_{23}|^2/|r_{12}|^2$. The other parameters are $\Lambda=1.5$ nm, $\lambda=9$ nm, $\theta_{23}-\theta_{12}=250°$, $\theta_{23}^{\downarrow}-\theta_{23}^{\uparrow}=20°$, and $|r_{23}^{\uparrow}|^2/|r_{23}^{\downarrow}|^2=1$.

$$\phi=\frac{1}{I}\sum_{n=1}(c_n-c_{n+1})|r_n|^2\phi_n, \tag{17}$$

where $|r_n|^2$, ε_n, and ϕ_n are respectively the reflectivity, the precession angle, and the rotation angle of a film with n completely filled monolayers, and where each of them is weighted with the layer coverage of the nth monolayer that is not yet covered in the actual film of thickness d, (c_n-c_{n+1}). We note that contributions of electron rays which enter the Au film at a position with a certain thickness and exit it after reflection at a position with a different thickness are neglected in our considerations.

2. $r_c \gg l$: Fully coherent model

The electron beam is considered now as being fully coherent. In this case, the total amplitude $r^{\uparrow,\downarrow}$ of the reflected beam is the sum of the amplitudes of the individual interferometers:

$$r^{\uparrow,\downarrow}=\sum_n (c_n-c_{n+1})r_n^{\uparrow,\downarrow}e^{in\delta_{ML}}, \tag{18}$$

where each reflection amplitude r_n of a film with n completely filled monolayers is weighted with the layer coverage of the nth monolayer that is not yet covered in the actual film of thickness d, (c_n-c_{n+1}). The above sum includes also a phase shift

$$\delta_{ML}=2k_{vac}d_{ML}\cos(45\,°), \tag{19}$$

with k_{vac} the wave vector of the electrons in vacuum and d_{ML} the thickness of a Au monolayer. We emphasize that one has to distinguish between Bragg (in-phase) and anti-Bragg (out-of-phase) conditions. While in the anti-Bragg condition $[\delta_{ML}=(2n+1)\pi]$ intensity oscillations with a period of 1 ML are expected, this is not the case in Bragg condition ($\delta_{ML}=2n\pi$). From $r^{\uparrow,\downarrow}$, we can then determine the reflectivity, the precession angle, and the rotation angle of the system.

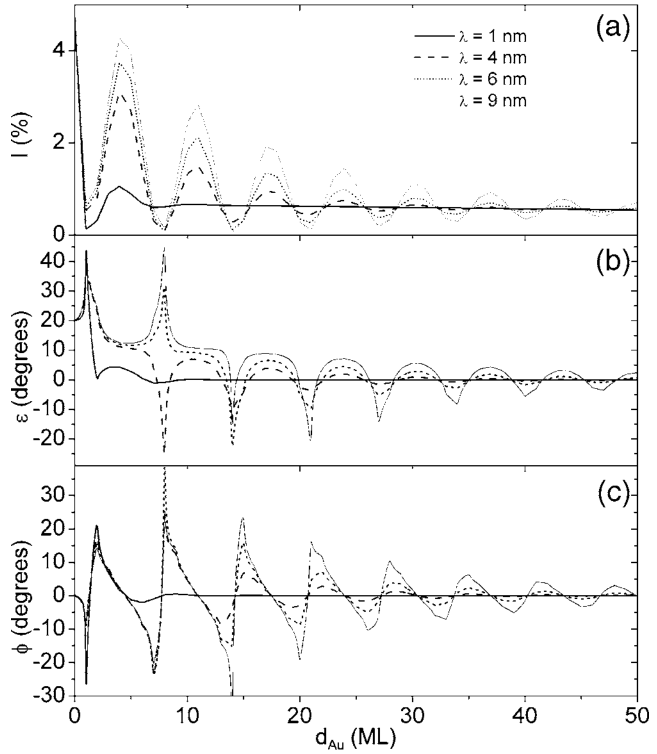

FIG. 11. As in Fig. 10, but now for different values of the inelastic mean free path λ. The other parameters are $\Lambda=1.5$ nm, $\theta_{23}-\theta_{12}=250°$, $\theta_{23}^{\downarrow}-\theta_{23}^{\uparrow}=20°$, $|r_{23}|^2/|r_{12}|^2=4$, and $|r_{23}^{\uparrow}|^2/|r_{23}^{\downarrow}|^2=1$.

C. Independent interferometers without intensity contribution of diffusively scattered electrons

In a first step to understand the behavior of both reflectivity and electron-spin motion, we consider only the model of independent interferometers and neglect for the moment any intensity contribution coming from elastic electrons being diffusively scattered (see Sec. VI E). Due to the scattering process, these electrons have lost their original phase information such that they cannot contribute to the interference. Figures 10 and 11 show the results of the Fabry-Pérot model for both reflectivity and electron-spin motion. We note that the curves show kinks due to the fact that the growth is assumed to be perfectly layerwise. In Sec. VI F, we will see how a change of the growth mode influences the behavior. For more realistic growth modes, we obtain smooth curves.

Here and in the following, the reflectivity of both the vacuum/Au interface, $|r_{12}|^2$, and of the Au/Co interface, $|r_{23}|^2=(|r_{23}^{\uparrow}|^2+|r_{23}^{\downarrow}|^2)/2$, are assumed to be small. In this case, only the value of the reflectivity ratio $|r_{23}|^2/|r_{12}|^2$ is important, while the exact value of $|r_{12}|^2$ has no influence on the behavior of the electron-spin motion angles. In the following, its value has been fixed to 0.5%. We note also that the parameters in Figs. 10 and 11 as well as in Figs. 12–14 and 16 are not chosen to behave like the data, but to illustrate the different behaviors of the spin-motion angles expected from the interference model when we vary a particular parameter.

For the sake of simplicity, we consider here only the influence of a spin-dependent phase gain at the Au/Co interface, i.e., $\theta_{23}^{\uparrow}\neq\theta_{23}^{\downarrow}$. The spin-dependent reflectivities, however, are assumed to be identical, i.e., $|r_{23}^{\uparrow}|^2=|r_{23}^{\downarrow}|^2$. Their influence will be described in the next section. We note a further simplification of our model in which we assume for the moment that both the spin-dependent phases $\theta_{23}^{\uparrow,\downarrow}$ and reflectivities $|r_{23}^{\uparrow,\downarrow}|^2$ are identical for the pure Co surface and the Au/Co interface. We will see in Sec. VI G, where simulations of the experimental data are shown, that this is by no means justified and that the values of the Au/Co interface can strongly deviate from those of the pure Co surface.

In Fig. 10, the reflectivity ratio $|r_{23}|^2/|r_{12}|^2$ is varied while all other parameters, in particular, the inelastic mean free path λ, are fixed. Let us first consider the behavior for the largest reflectivity ratio. Very strong changes appear as a function of Au film thickness. Most impressive is the behavior of the precession angle. Peaks in ε appear whenever the reflectivity is minimum, and become stronger in intensity and smaller in width the smaller the value of the reflectivity minimum is. Above a "critical" value of the Au film thickness, the peaks become dips. Now, their amplitude decreases and their width increases with increasing Au film thickness. What happens when we vary the reflectivity ratio? Figure 10 shows that the critical thickness shifts to smaller values with decreasing reflectivity ratio. While for a ratio of 6 we find three peaks in ε, two are seen for a ratio of 4, and only one for a ratio of 2. Finally, for a ratio of 1, only dips are obtained. Consequently, the observation of two peaks in ε at low electron energies in the experimental data leads us to conclude that the reflectivity of the Au/Co interface must be much larger than that of the vacuum/Au interface.

A similar behavior is found when we vary the inelastic mean free path λ instead of the reflectivity ratio (see Fig. 11). A smaller λ leads to a smaller critical thickness. Obviously, the two parameters play similar roles. Of course, if λ is too small, the oscillations become too strongly attenuated to be identified. The measurements of the precession angle at 10 and 11 eV electron energy (see Fig. 6) show a nice example of this behavior. While at 10 eV two peaks in ε are present, this is not the case anymore at 11 eV where one sees only one peak. Our simulations of the experimental data on the basis of the Fabry-Pérot model, which are partly presented in Sec. VI G, show, in fact, that this behavior is due to the strong change of λ (see Fig. 8).

D. Importance of the spin-dependent reflectivity

In the previous section, we assumed for simplicity that the spin-dependent reflectivities $|r_{23}^{\uparrow,\downarrow}|^2$ at the Au/Co interface were identical. Figure 12 shows now the behavior of both the reflectivity and the electron-spin motion when we allow for a spin dependence, i.e., $|r_{23}^{\uparrow}|^2\neq|r_{23}^{\downarrow}|^2$. While the reflectivity is nearly identical in the three cases, we note changes of both ε and ϕ with respect to the previous situation. The first one is a shift of the extrema so that the peaks in ε do not coincide anymore with the minima in reflectivity. The second one concerns the behavior of the rotation angle ϕ. While for identical reflectivities ϕ exhibits symmetric oscillations with respect to the abscissa, this is no more the case for different reflectivities. For lower thicknesses, ϕ is either mostly positive or negative. For larger thicknesses, however, one finds again rather symmetric oscillations. It is, thus, most probably the variation of the reflectivity ratio $|r_{23}^{\uparrow}|^2/|r_{23}^{\downarrow}|^2$ as a function of the electron energy which leads, in the experiment, to mostly negative values of the rotation angle at the higher electron energies, while at low energies, ϕ exhibits a symmetric behavior.

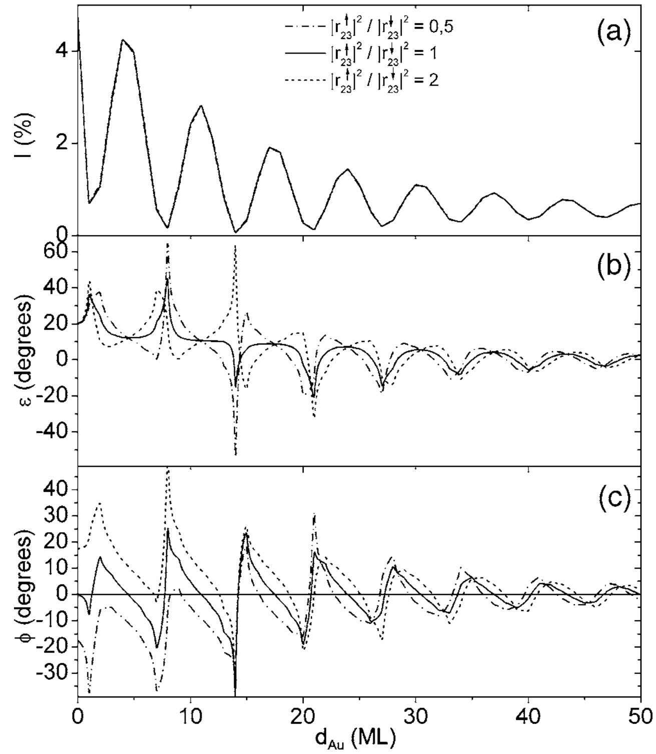

FIG. 12. As in Fig. 10, but now for different ratios of the spin-dependent reflectivity $|r_{23}^{\uparrow}|^2/|r_{23}^{\downarrow}|^2$ at the Au/Co interface. The other parameters are $\Lambda=1.5$ nm, $\lambda=9$ nm, $\theta_{23}-\theta_{12}=250°$, $\theta_{23}^{\downarrow}-\theta_{23}^{\uparrow}=20°$, and $|r_{23}|^2/|r_{12}|^2=4$.

In order to understand better the role of the spin-dependent reflectivity at the Au/Co interface, let us consider the case where the only spin dependence of the reflection amplitude $r_{23}^{\uparrow,\downarrow}$ comes from the reflectivity, i.e., the spin-dependent phase gains $\theta_{23}^{\uparrow,\downarrow}$ are identical. In Fig. 13, the ratio $|r_{23}^{\uparrow}|^2/|r_{23}^{\downarrow}|^2$ is chosen to be 1.9 (see curves I). We show also the behavior of the reflectivity and the electron-spin motion for the case where the spin dependence comes only from a spin-dependent phase gain, i.e., $\theta_{23}^{\uparrow}\neq\theta_{23}^{\downarrow}$ (see curves II). The comparison of the two situations reveals that the roles of ε and ϕ are interchanged. The rotation angle in situation I

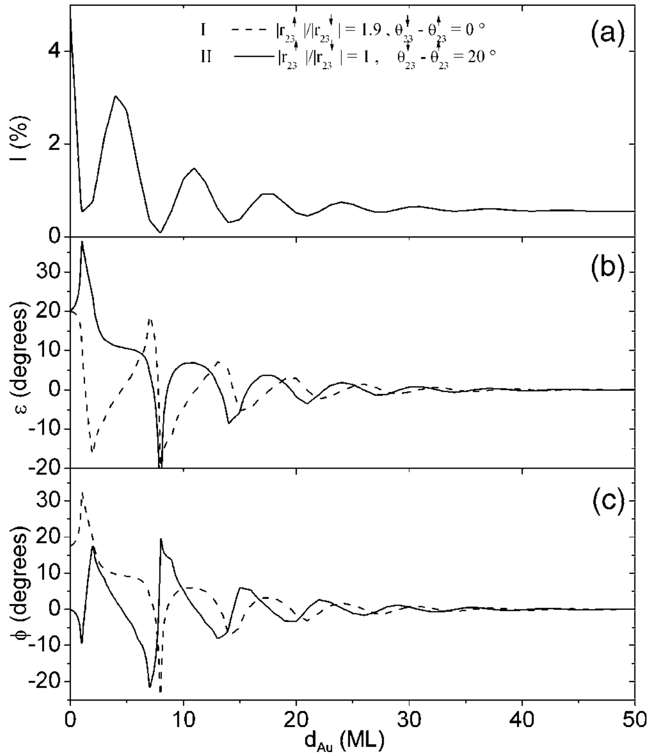

FIG. 13. As in Fig. 10. (I) $|r_{23}^{\uparrow}|^2 \neq |r_{23}^{\downarrow}|^2$ and $\theta_{23}^{\uparrow} = \theta_{23}^{\downarrow}$. (II) $|r_{23}^{\uparrow}|^2 = |r_{23}^{\downarrow}|^2$ and $\theta_{23}^{\uparrow} \neq \theta_{23}^{\downarrow}$. The other parameters are $\Lambda = 1.5$ nm, $\lambda = 4$ nm, $\theta_{23} - \theta_{12} = 250°$, and $|r_{23}|^2/|r_{12}|^2 = 4$.

exhibits now a behavior which is typical of the precession angle in situation II, and vice versa.

E. Inclusion of diffusively scattered electrons

Let us go back to the situation where the spin-dependent reflectivities $|r_{23}^{\uparrow;\downarrow}|^2$ are identical. However, now we assume the existence of an additional intensity contribution due to electrons having arbitrary phase being the result of a diffusive scattering process. Since we suppress inelastic electrons in our experiment, only scattered electrons having been subjected to (quasi)elastic interaction are detected. We note that elastically scattered electrons are concentrated in a very small cone around the original propagation direction, so that most of them can contribute to the measured intensity in specular geometry. Considering the very different epitaxial quality of the Co and Au films (see Sec. IV), we expect this intensity contribution to come predominantly from the Au film. In this case, the simplest expression for the intensity of the elastically scattered electrons is given by $I_s(d) = I_s^0(1 - e^{-2d/\lambda\,\cos(\alpha)})$, with I_s^0 a constant. Consequently, $I_s(d)$ will saturate for Au thicknesses larger than the information depth $\lambda\cos(\alpha)/2$.

By taking into account this additional intensity contribution, the expressions for the reflectivity and the spin-motion angles as a function of the Au film thickness read

$$I(d) = |r_{coh}(d)|^2 + I_s(d), \tag{20}$$

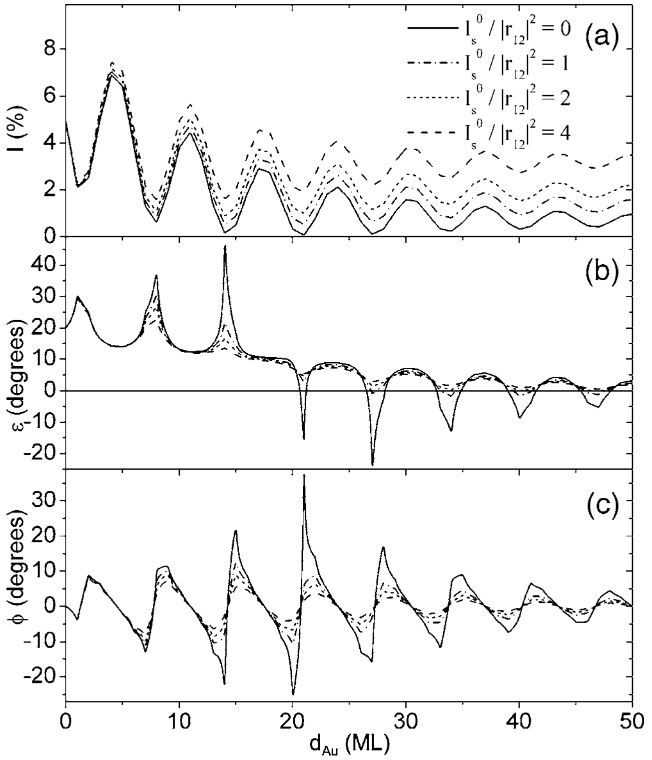

FIG. 14. Fabry-Pérot model (with independent interferometers and perfect layer-by-layer growth) with an additional intensity contribution due to elastically scattered electrons. (a) The reflectivity I, (b) the precession angle ε, and (c) the rotation angle ϕ are shown as a function of the Au film thickness for different values of $I_s^0/|r_{12}|^2$. The other parameters are $\Lambda = 1.5$ nm, $\lambda = 9$ nm, $\theta_{23} - \theta_{12} = 250°$, $\theta_{23}^{\downarrow} - \theta_{23}^{\uparrow} = 20°$, $|r_{23}|^2/|r_{12}|^2 = 8$, and $|r_{23}^{\uparrow}|^2/|r_{23}^{\downarrow}|^2 = 1$.

$$\varepsilon(d) = \frac{|r_{coh}(d)|^2\varepsilon_{coh}(d) + I_s(d)\varepsilon_{23}e^{-2d/\lambda\,\cos(\alpha)}}{I(d)}, \tag{21}$$

$$\phi(d) = \frac{|r_{coh}(d)|^2\phi_{coh}(d) + I_s(d)\phi_{23}e^{-2d/\lambda\,\cos(\alpha)}}{I(d)}, \tag{22}$$

where $|r_{coh}(d)|^2$, $\varepsilon_{coh}(d)$, and $\phi_{coh}(d)$ are respectively the reflectivity, the precession angle, and the rotation angle for the case without a diffusively scattered intensity contribution. Our assumption is that the portion of diffusively scattered electrons which have "seen" the magnetic Au/Co interface decreases with Au coverage in a simple exponential manner. Thus, the factor $e^{-2d/\lambda\,\cos(\alpha)}$ gives the fraction of the diffusively scattered intensity which contributes to the magnetic signal, i.e., to ε and ϕ. The quantities

$$\varepsilon_{23} = \theta_{23}^{\downarrow} - \theta_{23}^{\uparrow} \tag{23}$$

and

$$\phi_{23} = \arctan\left(\frac{|r_{23}^{\uparrow}|^2 - |r_{23}^{\downarrow}|^2}{2P_0|r_{23}^{\uparrow}||r_{23}^{\downarrow}|}\right) \tag{24}$$

would be the precession and the rotation angle, respectively, of the Au/Co interface which one would measure without interferences. We note that the two quantities ε_{23} and ϕ_{23} cannot be directly measured in an experiment as they are

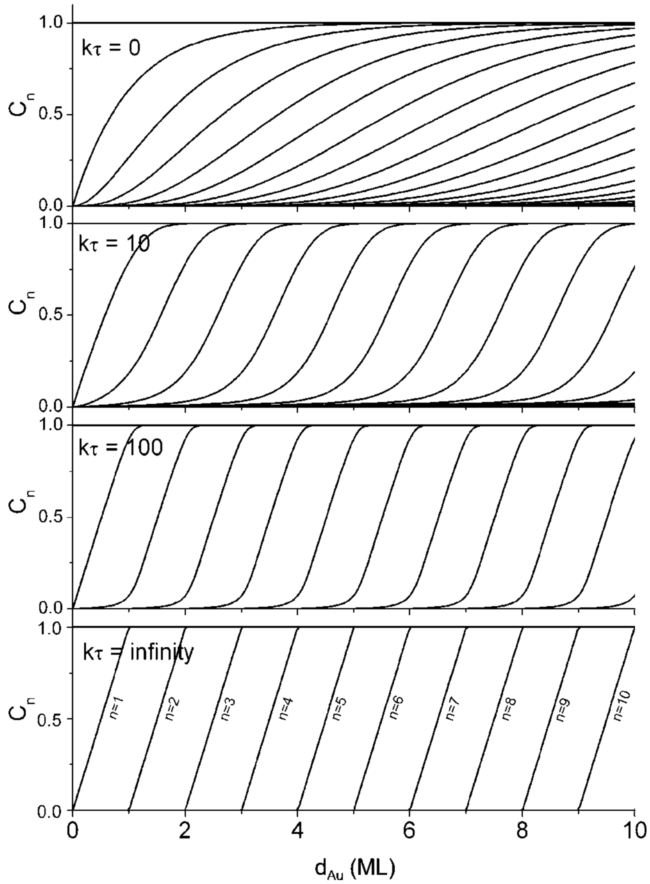

FIG. 15. The layer coverage c_n as a function of film thickness for different values of the quantity $k\tau$.

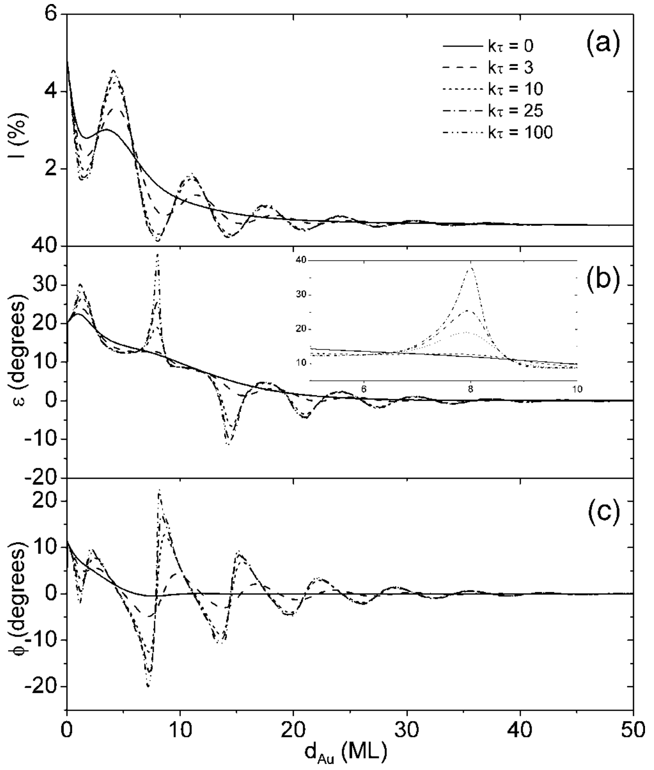

FIG. 16. Fabry-Pérot model with independent interferometers. (a) The reflectivity I, (b) the precession angle ε, and (c) the rotation angle ϕ are shown as a function of the Au film thickness for different quantities $k\tau$. The other parameters are $\Lambda=1.5$ nm, $\lambda=4$ nm, $\theta_{23}-\theta_{12}=250°$, $\theta_{23}^{\downarrow}-\theta_{23}^{\uparrow}=20°$, $|r_{23}|^2/|r_{12}|^2=8$, $|r_{23}^{\uparrow}|^2/|r_{23}^{\downarrow}|^2=1.5$, and $I_s^0/|r_{12}|^2=0$. The inset is a zoom.

always superimposed by the quantum interference effect. They can only be deduced from a fit of the experimental data on the basis of the interferometer model as we did in our earlier study of the Cu/Co(001) system.[6]

We readily see how important the inclusion of diffusively scattered electrons is in order to understand our experimental data. In the case without diffusively scattered electrons, the amplitude of the peaks in ε increases on approaching the critical thickness, a behavior which is not observed in our experiments. Instead, the amplitude decreases as found in the Fabry-Pérot model when we include diffusively scattered electrons (see Fig. 14). A further aspect of the experimental data finds now also its explanation. While in the case without diffusively scattered electrons ε exhibits, for Au coverages above the critical thickness, more or less symmetric oscillations with respect to the abscissa, this is not the case when we include a contribution of diffusively scattered electrons (which in the following is expressed in units of $|r_{12}|^2$): the precession angle is mostly positive (if $\varepsilon_{23}>0$) as shown in Fig. 14.

F. Importance of the growth mode

Up to now, we assumed a perfect layer-by-layer growth of the Au film on top of the Co(001) substrate. In this section, we will analyze the influence of the growth mode on the behavior of the electron-spin motion as a function of the Au thickness. For the growth of Au on Co, we assume the model of Cohen *et al.*,[26] which has been developed to explain the intensity oscillations which are observed in many reflection high-energy electron diffraction experiments as a function of film thickness.

Starting from the assumption that an atom which is covered by one or more atoms cannot diffuse anymore, the layer coverage c_n of the nth monolayer as a function of time t reads[26]

$$\frac{dc_n}{dt}=\frac{1}{\tau}(c_{n-1}-c_n)+k(c_{n+1}-c_{n+2})(c_{n-1}-c_n)-k(c_n-c_{n+1})\times(c_{n-2}-c_{n-1}), \tag{25}$$

with τ the time for the growth of one 1 ML and k the diffusion rate. The first term is due to the nondiffusive growth on top of the $(n-1)$th monolayer, the second one to atoms diffusing from the $(n+1)$th to the nth monolayer, and the third one to atoms diffusing from the nth to the $(n-1)$th monolayer. This system of nonlinear equations can be solved numerically using the following initial conditions: $c_0(t)=1$ and $c_n(0)=0$. Figure 15 shows the layer coverage c_n as a function of the film thickness for different values of the quantity $k\tau$. While the case of nondiffusive growth is represented by $k\tau=0$, perfect layer-by-layer growth is found for $k\tau\to\infty$.

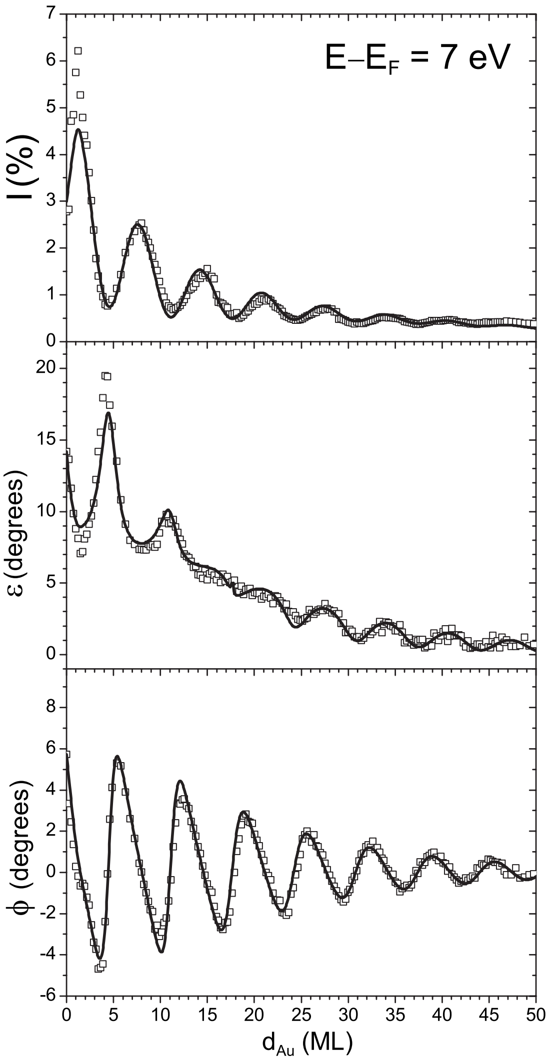

FIG. 17. Quantum-size oscillations of the spin motion as a function of the Au overlayer thickness at the electron energy $E-E_F=7$ eV (top: spin-integrated reflectivity I, middle: precession angle ε, and bottom: rotation angle ϕ). Beside the experimental data (symbols), a simulation based on the Fabry-Pérot interferometer model in the fully coherent limit and with a contribution $I_s^0/|r_{12}|^2=3$ of diffusively scattered electrons is shown. The other parameters are $\Lambda=1.5$ nm, $\lambda=8.2$ nm, $\theta_{23}-\theta_{12}=66°$, $\theta_{23}^{\downarrow}-\theta_{23}^{\uparrow}=12°$, $|r_{23}|^2/|r_{12}|^2=7$, and $|r_{23}^{\uparrow}|^2/|r_{23}^{\downarrow}|^2=1.04$.

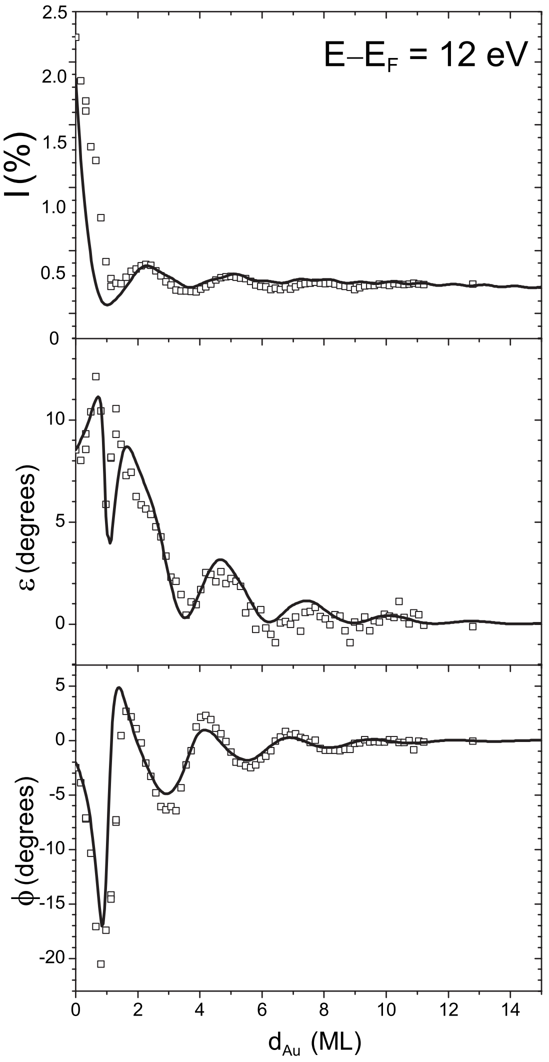

FIG. 18. As in Fig. 17 at the electron energy $E-E_F=12$ eV. The intensity contribution of diffusively scattered electrons is $I_s^0/|r_{12}|^2=0.5$. The other parameters are $\Lambda=0.58$ nm, $\lambda=1.45$ nm, $\theta_{23}-\theta_{12}=-45°$, $\theta_{23}^{\downarrow}-\theta_{23}^{\uparrow}=20°$, $|r_{23}|^2/|r_{12}|^2=0.4$, and $|r_{23}^{\uparrow}|^2/|r_{23}^{\downarrow}|^2=0.49$.

We will consider the influence of the growth mode only in the model of independent interferometers (see Sec. VI B), each of them having a thickness which is an integer number of a monolayer. The reflectivity and the spin-motion angles can then be determined by using Eqs. (15)–(17). Figure 16 shows both the reflectivity and the electron-spin motion for different values of the growth quantity $k\tau$. The inset in Fig. 16 shows that the second peak in ε is particularly sensitive on the growth mode. This is due to the fact that this peak has quite a small width in comparison to the other structures and is, therefore, much more strongly influenced by an increase of the film roughness. For too small values of $k\tau$, the oscillations completely disappear. We emphasize that this sensitivity of the intensity and the spin-motion angles on $k\tau$ allows a rough determination of the latter.

G. Simulations of the experimental data based on the interferometer model

In this section, simulations of the experimental data based on the Fabry-Pérot interferometer model are shown. We emphasize that, although not few parameters are involved, we have quite good confidence in the simulations as they are done simultaneously with three different quantities, namely, the intensity and the two spin-motion angles. Although most of the data are already quite well represented in the model of independent interferometers, certain features can only be explained in the fully coherent model in which the interference of regions differing in thickness by a multiple of 1 ML has to be considered. An example are the structures at a thickness of around 1 ML both in ε and ϕ at $E-E_F=12$, 13, and 15 eV. Thus, in the following, we will show only simulations

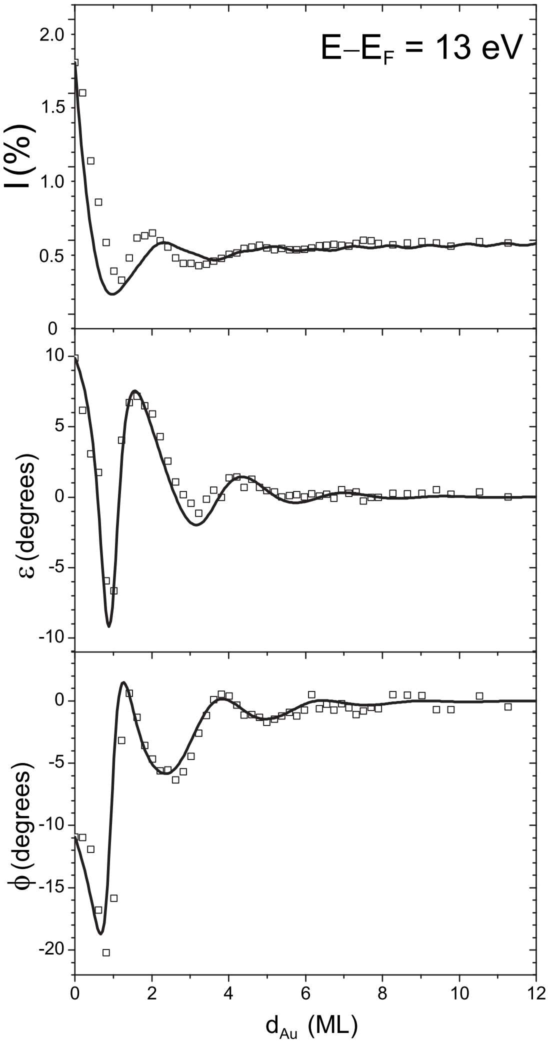

FIG. 19. As in Fig. 17 at the electron energy $E-E_F=13$ eV. The intensity contribution of diffusively scattered electrons is $I_s^0/|r_{12}|^2=0.4$. The other parameters are $\Lambda=0.57$ nm, $\lambda=0.9$ nm, $\theta_{23}-\theta_{12}=-50°$, $\theta^{\downarrow}_{23}-\theta^{\uparrow}_{23}=10°$, $|r_{23}|^2/|r_{12}|^2=0.4$, and $|r^{\uparrow}_{23}|^2/|r^{\downarrow}_{23}|^2=0.28$.

in the fully coherent model. We note that for all simulations the growth parameter $k\tau$ has been fixed to 15. Using much smaller (<8) as well as much larger values (>30) of $k\tau$ yield a significantly less good correspondence between experiment and simulation.

As already noted in Sec. VI B, in the fully coherent model, one has to distinguish between Bragg and anti-Bragg conditions. Since short period oscillations of the order of 1 ML cannot be identified in the data,[27] we conclude that most of the detected electrons in our experiments are the result of an in-phase (Bragg) scattering process.

Figures 17–19 show the experimental data for $E-E_F=7$, 12, and 13 eV together with simulations based on the interferometer model. Assuming $I_s^0/|r_{12}|^2=3$ for 7 eV, 0.5 for 12 eV, and 0.4 for 13 eV, parameters are found which describe quite well the intensity as well as the spin-motion angles ε and ϕ. Quite interesting is the behavior of ε for $E-E_F=12$ eV. The ε data at a coverage of about 1 ML seem to be a superposition of a peak and a dip. As already noted, this behavior cannot be explained within the model of independent interferometers.

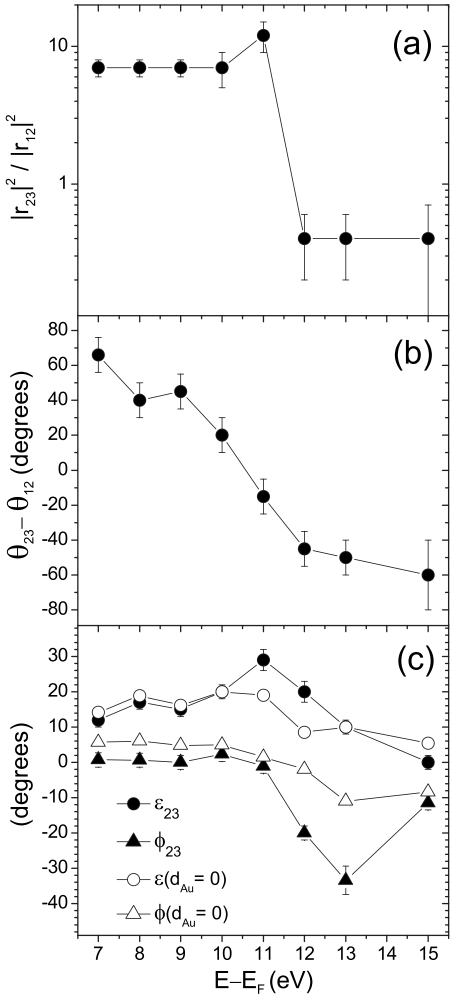

FIG. 20. Values of (a) the reflectivity ratio $|r_{23}|^2/|r_{12}|^2$, (b) the phase difference $\theta_{23}-\theta_{12}$, and (c) ε_{23}, ϕ_{23}, $\varepsilon(d_{\mathrm{Au}}=0)$, and $\phi(d_{\mathrm{Au}}=0)$ as a function of the electron energy deduced from the interferometer model. The lines are guides for the eye.

We emphasize that the study of both reflectivity and spin-motion angles in the Au/Co system and its analysis within the above Fabry-Pérot interferometer model allow a study of the buried magnetic Au/Co interface. In Fig. 20(a), the reflectivity ratio $|r_{23}|^2/|r_{12}|^2$ of the buried Au/Co interface is shown. As for the Cu/Co interface which has recently been studied by us,[6] the ratio exhibits quite small values for electron energies above $E-E_F=12$ eV, while it is by 1 order of magnitude larger for lower energies, which is due to a gap in the electronic band structure of Co(001) along the Γ-X direction in reciprocal space. We note that it is difficult to determine $|r_{23}|^2$ as the purely coherent part of the reflectivity $|r_{12}|^2$ of the Au surface cannot directly be measured.

The phase shift of the reflected electron wave with respect to the incident wave is known to change dramatically on traversing a band gap.[28] Thus, we expect to see a strong change of the phase θ_{23} when we cross the band gap of Co(001) for energies below 12 eV. Assuming only small variations of the phase θ_{12} of the vacuum/Au interface in the investigated energy range, the phase difference $\theta_{23}-\theta_{12}$ should behave in the same manner. The latter assumption is justified because no band gap can be identified for Au between 7 and 15 eV. In fact, if there were a band gap, it would give rise to a drastic increase of the period Λ of the quantum-well oscillations followed by a decrease for energies beyond the gap. However, Λ shows a monotonic behavior as a function of energy (see Fig. 8).

Figure 20(c) shows ε_{23}, ϕ_{23}, $\varepsilon(d_{\mathrm{Au}}=0)$, and $\phi(d_{\mathrm{Au}}=0)$ as a function of electron energy. While the first two quantities determine the behavior of the buried interface, the latter two reflect the behavior of the pure Co surface. Both for ε_{23} and ϕ_{23} we find a much more pronounced structure for the Au/Co interface than for the pure Co surface. Whether this is due to the Au coverage, which is very likely to influence the magnetic characteristics of the Co film, the changed angle of incidence at the Au/Co interface with respect to that of the vacuum/Co interface, or both, cannot be said as long as measurements with a variable angle of incidence cannot be realized with our experimental setup.

VII. CONCLUSION

The reflectivity and the electron-spin motion, i.e., the precession angle and the rotation angle, have been studied in the quantum-well system Au/Co(001) by spin-polarized electron reflection experiments. All three investigated quantities exhibit an oscillatory behavior as a function of the Au film thickness. We explain the observed behavior on the basis of the Fabry-Pérot interferometer model. The different roles of the reflectivity ratio $|r_{23}|^2/|r_{12}|^2$, the inelastic mean free path λ, the spin-dependent reflectivity $|r_{23}^{\uparrow,\downarrow}|^2$ at the Au/Co interface, the contribution of diffusively scattered electrons, and the growth mode have been elucidated. We have demonstrated that all three measured quantities can be well described within the interferometer model, and that this fact can be exploited to study the spin-dependent reflection properties of the buried Au/Co interface.

---

[1] M. Milun, P. Pervan, and D. P. Woodruff, Rep. Prog. Phys. **65**, 99 (2002), and references therein.

[2] S. S. P. Parkin, N. More, and K. P. Roche, Phys. Rev. Lett. **64**, 2304 (1990).

[3] P. Bruno, Y. Suzuki, and C. Chappert, Phys. Rev. B **53**, 9214 (1996).

[4] C. H. Back, W. Weber, A. Bischof, D. Pescia, and R. Allenspach, Phys. Rev. B **52**, R13114 (1995).

[5] W. Weber, A. Bischof, R. Allenspach, C. Wursch, C. H. Back, and D. Pescia, Phys. Rev. Lett. **76**, 3424 (1996).

[6] L. Joly, L. Tati-Bismaths, and W. Weber, Phys. Rev. Lett. **97**, 187404 (2006).

[7] R. E. Thomas, J. Appl. Phys. **41**, 5330 (1970).

[8] D. Oberli, R. Burgermeister, S. Riesen, W. Weber, and H. C. Siegmann, Phys. Rev. Lett. **81**, 4228 (1998).

[9] W. Weber, D. Oberli, S. Riesen, and H. C. Siegmann, New J. Phys. **1**, 9.1 (1999).

[10] W. Weber, S. Riesen, and H. C. Siegmann, Science **291**, 1015 (2001).

[11] W. Weber, S. Riesen, C. H. Back, A. Shorikov, V. Anisimov, and H. C. Siegmann, Phys. Rev. B **66**, 100405(R) (2002).

[12] L. Joly, J. K. Ha, M. Alouani, J. Kortus, and W. Weber, Phys. Rev. Lett. **96**, 137206 (2006).

[13] M. P. Seah and W. A. Dench, Surf. Interface Anal. **1**, 2 (1979).

[14] Z. Q. Qiu, J. Pearson, and S. D. Bader, Phys. Rev. B **46**, 8659 (1992).

[15] Y. G. Shen, J. Yao, D. J. O'Connor, B. V. King, and R. J. MacDonald, J. Phys.: Condens. Matter **8**, 4903 (1996).

[16] F. Scheurer, R. Allenspach, P. Xhonneux, and E. Courtens, Phys. Rev. B **48**, 9890 (1993).

[17] S. G. J. Mochrie, D. M. Zehner, B. M. Ocko, and D. Gibbs, Phys. Rev. Lett. **64**, 2925 (1990).

[18] H. Bulou and C. Goyhenex, Phys. Rev. B **65**, 045407 (2002).

[19] M. A. Mueller, T. Miller, and T. C. Chiang, Phys. Rev. B **41**, 5214 (1990).

[20] J. E. Ortega and F. J. Himpsel, Phys. Rev. Lett. **69**, 844 (1992).

[21] J. E. Ortega, F. J. Himpsel, G. J. Mankey, and R. F. Willis, Phys. Rev. B **47**, 1540 (1993).

[22] R. K. Kawakami, E. Rotenberg, H. J. Choi, E. J. Escorcia-Aparicio, M. O. Bowen, J. H. Wolfe, E. Arenholz, Z. D. Zhang, N. V. Smith, and Z. Q. Qiu, Nature (London) **398**, 132 (1999).

[23] S. Egger, C. H. Back, J. Krewer, and D. Pescia, Phys. Rev. Lett. **83**, 2833 (1999).

[24] G. Borstel and M. Wohlecke, Phys. Rev. B **28**, 3153 (1983).

[25] H. Kanter, Phys. Rev. B **1**, 522 (1970).

[26] P. I. Cohen, G. S. Petrich, P. R. Pukite, G. J. Whaley, and A. S. Arrott, Surf. Sci. **216**, 222 (1989).

[27] In fact, the Fabry-Pérot interferometer model shows that in anti-Bragg condition, short period oscillations in ε and ϕ of exactly 1 ML period appear only if the long period is infinite. For finite values of the long period, the short period increases. The intensity, of course, shows, in addition to the short and long periods, a third one which is exactly 1 ML.

[28] J. B. Pendry and S. J. Gurman, Surf. Sci. **49**, 87 (1975).